

# Wind tunnel testing of a swept tip shape and comparison with multi-fidelity aerodynamic simulations

Thanasis Barlas, Georg Raimund Pirrung, Néstor Ramos-García, Sergio González Horcas, Robert Flemming Mikkelsen, Anders Smærup Olsen, and Mac Gaunaa

DTU Wind Energy, Frederiksborgvej 399, 4000 Roskilde, Denmark

**Correspondence:** Thanasis Barlas (tkba@dtu.dk)

## Abstract.

One promising design solution for increasing the efficiency of modern horizontal axis wind turbines is the installation of curved tip extensions. However, introducing such complex geometries may move traditional aerodynamic models based on Blade Element Momentum (BEM) theory out of their range of applicability. This motivated the present work, where a swept tip shape is investigated by means of both experimental and numerical tests. The latter group accounted for a wide variety of aerodynamic models, allowing to highlight the capabilities and limitations of each of them in a relative manner. The considered swept tip shape is the result of a design optimization, focusing on locally maximizing power performance within load constraints. For the experimental tests, the tip model is instrumented with spanwise bands of pressure sensors and is tested in the Poul la Cour wind tunnel at the Technical University of Denmark (DTU). The methods used for the numerical tests consisted of a blade element model, a near-wake model, lifting-line free-wake models, and a fully resolved Navier-Stokes solver. The comparison of the numerical and the experimental tests results is performed for a given range of angles of attack and wind speeds, which is representative of the expected conditions in operation. Results show that the blade element model cannot predict the measured normal force coefficients, but the other methods are generally in good agreement with the measurements in attached flow. Flow visualization and pressure distribution compare well with Computational Fluid Dynamics (CFD) simulations. The agreement in the clean case is better than in the tripped case at the inboard sections. Some uncertainties regarding the effect of the boundary layer at the inboard tunnel wall and the post stall behavior remain.

*Copyright statement.* Creative Commons Attribution 4.0 License

## 1 Introduction

The trend of reducing the Levelized Cost of Energy (LCOE) of horizontal axis wind turbines through increasing rotor size has long been established. To achieve this, the challenges of scale must be overcome through innovative turbine design and control strategies (Veers et al., 2019). One promising blade design concept is advanced aeroelastically optimized blade tip extensions, which could drive rotor upscaling in a modular and cost effective way. Such designs can be aligned with the wind

turbine manufacturers' trend to offer modular platform options for facilitating site-specific sales. Different tip designs would be a potential solution with a reduced investment cost compared to a new family of blades.

25 Traditional aircraft related bibliography (e.g. see (Hoerner et al., 1975)) covers most of the aerodynamic aspects of winglets and swept wing tip shapes, but the specific design space and objectives of wind turbine applications require distinct research efforts even considering non-rotating setups, as in this work. Existing research work relevant to wind turbine applications typically focuses on winglets and aerodynamic tip shapes, with limited testing in controlled conditions (Johansen et al., 2006; Gaunaa et al., 2007; Gertz et al., 2012; Hansen et al., 2018). Moreover, there is no relevant research work focusing on details  
30 of tip shape aerodynamics relevant to the application of tip extensions for blade upscaling. Most of the published work on tip shapes for wind turbine blades focuses on small tip modifications (mainly winglets) which only modify the tip vortex characteristics. This work focuses on aerodynamics of blades with generalized curved shapes (see Fig. 1). In the present work,

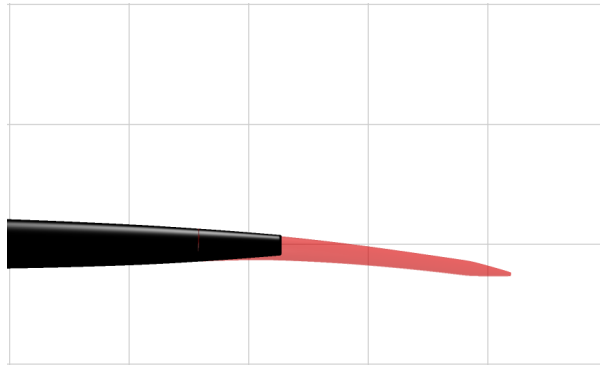


**Figure 1.** Example tip shape applied on a wind turbine blade (Barlas et al., 2020).

the aerodynamics of a curved tip shape is investigated via wind tunnel experiments and numerical modeling. The considered swept tip shape is the result of design optimization, focusing on locally maximizing power performance within load constraints  
35 compared to an optimal straight tip, for testing in an outdoor rotating test rig (RTR). The tip model is instrumented with spanwise bands of pressure sensors and is tested in the Poul la Cour wind tunnel at the Technical University of Denmark (DTU), for a range of angle of attack and wind speed. Aerodynamic models of different fidelities are utilized to simulate the wind tunnel cases and are compared with the measurement data, namely a blade element model, a near-wake model, lifting-line free-wake models, and a fully resolved Navier-Stokes solver.

## 40 2 Tip model design

The tip shape presented in this work is the result of an aeroelastic optimization for maximizing power performance within load constraints for a tip mounted on DTU's rotating test rig (RTR) (Madsen et al., 2015; Ai et al., 2019). The tested tip shape in this work is a scaled version of that aeroelastic tip prototype (publication pending). The optimization method used is the same as the one described in (Barlas et al., 2020), used for the tip design of a full scale wind turbine. The method of

45 optimizing the tip for the RTR is essentially the same, while the baseline geometry and load envelope is defined by a reference straight tip, designed for an optimal BEM performance. The reference tip was designed using the FFA-W3-211 airfoil with fully turbulent wind tunnel polars (Bertagnolio et al., 2001) at a Reynolds number of  $1.78e6$  (Fig. 2). A predefined length of

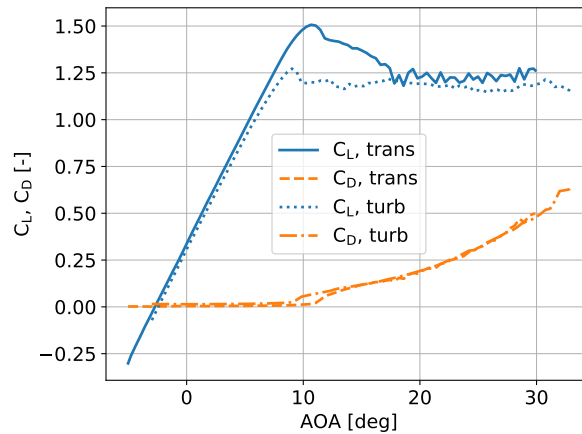


**Figure 2.**  $C_L$  and  $C_D$  versus angle of attack for the FFA-W3-211 airfoil in free transition and fully turbulent conditions (KTH wind tunnel data (Bertagnolio et al., 2001)).

3m was used as a design constraint for an outdoor rotating test rig and where the tip is mounted on a 8m cylindrical boom. The chord and twist distributions of the straight tip were determined from BEM performance for optimal power coefficient in operation at 30rpm and 6m/s inflow wind speed. The resulting aeroelastically optimized tip utilizing sweep, achieved a 19.58% increase in power with the same ultimate flapwise bending moment at the boom root and tip connection as the baseline. The design was evaluated with the near wake model in the aeroelastic code HAWC2 (Larsen and Hansen, 2007) for an extreme turbulence case (class III-C) at a wind speed of 6m/s. Compared to the reference straight tip, the design features a highly swept (in-plane offset) centerline (Fig. 3), a slender chord distribution, and a negative twist distribution towards feather (Fig. 4).  
55 All coefficients are normalized by the wind tunnel speed for simplicity, even though the relative velocity at the cross sections differs. The coefficients are shown as function of the angle of attack at the root section. The local AOA differs due to the twist distribution.

The geometry of the optimal tip is scaled with a factor of 0.5 compared to the RTR tip dimensions in order to be accommodated in the Poul la Cour wind tunnel (PLCT) at DTU (Fig. 5). The wind tunnel speed is tuned accordingly in order to achieve the same range of Reynolds numbers compared to operation on the RTR ( $0.8e6$ - $1.5e6$ ). The corresponding Mach numbers are very low for all cases (0.05-0.17) so the flow is considered incompressible.  
60

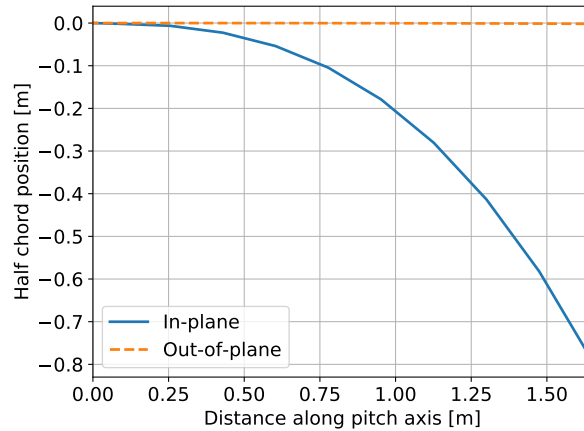


**Figure 3.** Centerline of the tip design.

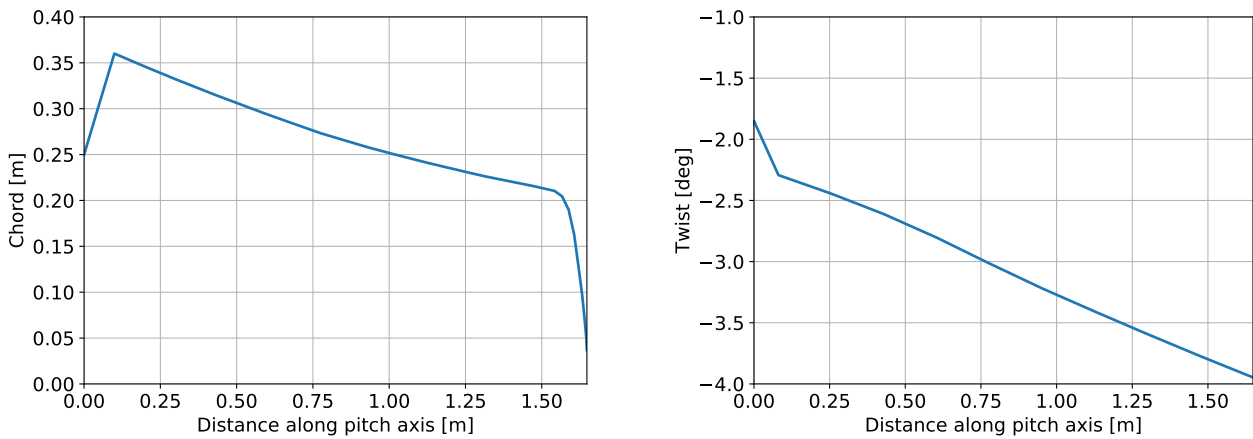


**Figure 4.** Planform of the tip design.

### 3 Wind tunnel test setup

The PLCT is a closed return tunnel with a closed test section. When testing the tip, the test section uses an aerodynamic setup with hard walls. The rectangular test section has the dimensions of height,  $H=2.0\text{m}$ , width,  $W=3.0\text{m}$  and length,  $L=9.0\text{m}$ . The effective contraction ratio of 9 and the system of screens and Honeycomb results in a low turbulence level of  $Tu < 0.1\%$  for a frequency range of 10–5000 Hz and a flow velocity of 50 m/s. The turntables have a diameter of 1.355m, with a 0.5m x 1.25m hatch with rounded corners. The center of the turntables are located 4 m downstream of the contraction. The tip is mounted in the upper turntable (Fig. 6).

The pressures measured from surface pressure taps in the model are numerically integrated to determine the normal and tangential force components. The data acquisition (DAQ) system is based upon the CompactRIO system from National In-

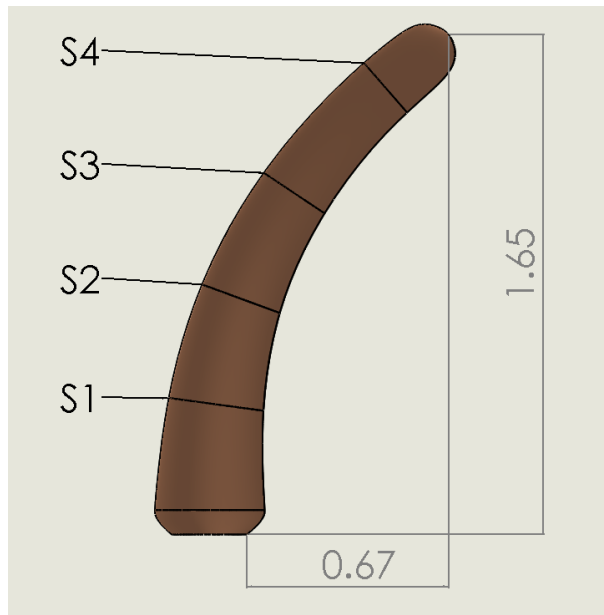


**Figure 5.** 3D geometry of the tip (in meters), indicating the 4 sections where pressure taps are located.



**Figure 6.** The tip model mounted in the test section of the Poul la Cour wind tunnel.

struments and a DTU in-house made LabView program. The pressures are measured with Scanivalve MPS4264 scanners with full scale ranges from 6.9kPa to 69 kPa (the highest ranges are used close to the leading edge). The accuracy for all scanners is 0.06% of the full scale range (0.0041 kPa to 0.041 kPa). The actual accuracy is in practice much better, especially for the higher ranges. In previous studies, the standard deviation of the pressures for attached flow was found to be small, and it is assumed that this is the case for the current measurements as well.

Each of the four sections is equipped with 32 pressure taps. The same normalised chordwise positions are used on all four sections. In the leading edge region (the first 10% of the chord) 14 taps are distributed evenly along the arc length. On the remaining 90% of the chord, nine taps are distributed on each side. Again, they are equally distributed along the arc length. The last tap is located at approximately 90% chord on each side. In the post-processing a point at 100% of the chord is added where the pressure is assumed to be the average of the pressures at the last tap on each side. The present method is used as a first estimation due to its simplicity and robustness. In any case, the influence from the extrapolation method on the normal force is minor, whereas the effect on the tangential force can be larger, but still within acceptable limits.

The tip is tested in a range of wind speeds, angles of attack and surface conditions, as shown in Table 1.

Wind speed [m/s]	Surface condition	AOA range [deg]	Reynolds nr [-]
20	clean	-180:1:+180	$4.8 \cdot 10^5 - 2.6 \cdot 10^5$
40	clean	-180:1:+180	$9.6 \cdot 10^5 - 5.3 \cdot 10^5$
60	clean	-20:1:+20	$1.4 \cdot 10^6 - 8.0 \cdot 10^5$
20	tripped	-180:1:+180	$4.8 \cdot 10^5 - 2.6 \cdot 10^5$
40	tripped	-180:1:+180	$9.6 \cdot 10^5 - 5.3 \cdot 10^5$
60	tripped	-20:1:+20	$1.4 \cdot 10^6 - 8.0 \cdot 10^5$

**Table 1.** Test configurations. Tripped; zz-tape (0.205mm height, 6mm wide, 70 deg along the entire span)

at 5%c on suction side and 10%c on pressure side.

#### 4 Numerical simulations

The different aerodynamic models used for the numerical simulations, together with the corresponding setups, are described in this section. Based on the labels used in the present document, those could be ordered in terms of fidelity as: HAWC2 (blade element model), HAWC2 near wake, MIRAS (free wake lifting line) and EllipSys3D (CFD). In addition to these models, a different lifting line code, LLTunnel, was utilized as part of this work for evaluating the effect of the wind tunnel, which was not fully included in any of the previous models. In terms of fidelity, LLTunnel could be thought of as lying between HAWC2 near wake and MIRAS, because it is not a free wake method. However, it does model the full interference effect of the tunnel on the aerodynamic response. Both EllipSys3D and MIRAS correspond to independent fluid dynamics solvers. Those two codes were run in the present study through the external coupling framework referred to as *DTU coupling* (Horcas et al., 2020; Ramos et al., 2020). In this way, the results were integrated in the aeroelastic solution of HAWC2. It should be remarked that

the stiff nature of the studied tip made this integration unnecessary from the results point of view. Nevertheless, the use of the DTU coupling framework ensured the consistency of the studied tip geometries, as well as the direct comparability of the outputs presented in this work. In particular the integrated forces for several cross sections, which were perpendicular to the mid chord line.

#### 4.1 Simulated Geometries

The tunnel wall at the root section is 43 centimeters away from the innermost instrumented section on the model. In the tunnel, this wall will 1) prevent the formation of a strong root vortex and 2) create a boundary layer at the root wall which will cause the velocity to decrease towards zero in its vicinity. To model the first effect of the wall on the trailed vorticity behind the tip, a mirrored tip is simulated in all codes except for LLTunnel. This is achieved by mirroring the tip geometry at the root section in HAWC2 near wake and MIRAS. A flat plane with a symmetry condition is added in EllipSys3D. The blade element method in HAWC2 will not see any effect of mirroring due to the missing cross sectional aerodynamic coupling. In contrast to the other codes, LLTunnel models the effect of all four tunnel walls using the method of mirror images.

#### 4.2 HAWC2 and HAWC2 near wake

BEM, which can otherwise be used to compute the induced velocity at a rotor disc, is not applicable in the present study. The single tip configuration resembles more closely a blade in standstill than a rotor in operation. In this case only the blade element part of blade element momentum theory is applicable. The wind speed is projected into the airfoil cross sections, relative velocity and angle of attack are computed and lift, drag and moment coefficients are interpolated from airfoil polar tables. A tip loss model typically used in BEM is not relevant, because no rotor induction is present, and all the sections are radially independent. Results from this basic blade element approach are labeled 'HAWC2' in the following.

The near wake model, a simplified lifting line model (Pirrung et al., 2016, 2017a), was previously extended to standstill conditions to provide induction modeling where BEM theory is not applicable (Pirrung et al., 2017b). This model computes the cross sectional aerodynamic coupling through the trailed vortex, which will for a single tip mainly result in strong vortices trailed from the root and tip sections. The near wake model was recently extended to model swept blades in operation (Li et al., 2018), but this extension is not yet available for stand still cases. So the geometry of the wake in the 'HAWC2 near wake' (or simply HAWC2 NW) computations is that of a straight wake behind a straight tip. The relative velocities and AOA at each section are though computed by projecting the wind speed into the airfoil cross sections of the swept tip as in the 'HAWC2' case described above. The tip was discretized into aerodynamic sections and vortex trailing points at the root, tip and in between sections according to a cosine distribution.

#### 4.3 MIRAS

Simulations with the multi-fidelity vortex solver MIRAS (Ramos et al., 2016, 2017, 2019) have been carried out, using a built-in lifting line (LL) aerodynamic module in combination with a free-wake filament based model.

125 In what follows, a description of the LL free-wake model employed in all the HAWC2-MIRAS simulations is detailed. In the model, the blades are represented by discrete vortex rings along the span. These elements account for the bound vortex strength and release vorticity into the flow. The bound vortex is discretized with 80 equally spaced straight segments in the mirrored "c-shaped" configuration. The leading segments of the bound vortex rings are placed along the blade quarter chord line, with the collocation point located at the three-quarter chord.

130 The strength of these vortex filaments is calculated via the Kutta-Joukowski theorem,  $\bar{\Gamma}$ ,

$$\bar{\Gamma} = \frac{\bar{L}}{\rho \bar{V}_{cp}} \quad (1)$$

where  $L$  is the lift force of each aerodynamic section, obtained by interpolation in a set of tabulated airfoil data ( $C_l, C_d, C_m$ ) as function of the computed angle of attack.  $\rho$  is the air density at a given temperature and  $V_{cp}$  is calculated as follows,

$$\bar{V}_{cp} = \bar{V}_0 + \bar{u}_w + \Delta \bar{u}^b \quad (2)$$

135 where  $\bar{V}_0$  is the free-stream velocity,  $\bar{u}_w$  is the wake induced velocity, and  $\Delta \bar{u}^b$  accounts for the curved bound vortex influence as detailed in Li et al. (2020).

The motion of the rest of the filaments is described by Lagrangian fluid markers placed at the filament end points. The filaments are therefore convected downstream with a velocity, which includes the contribution from the free-stream, the bound vorticity and the wake induction. The induced velocities are calculated directly by evaluating the Biot-Savart law. To desingularize the Biot-Savart law, the Scully et al. (1972) vortex core profile is applied to all the released vortex filaments. In this way, an approximation to viscous diffusion, vortex core growth and vortex straining can be included into the inviscid wake model.

140 Pitch angles from -5 to 20 degrees with a pitch step of 1 degree have been simulated. A time step of 0.001 s is used, with 300 time steps between pitch increments. The total number of filament rows used to represent the wake is fixed at 300, as shown in Figure 7. A total of 7800 time steps have been computed per simulation. Note that the model is considered rigid in this study.

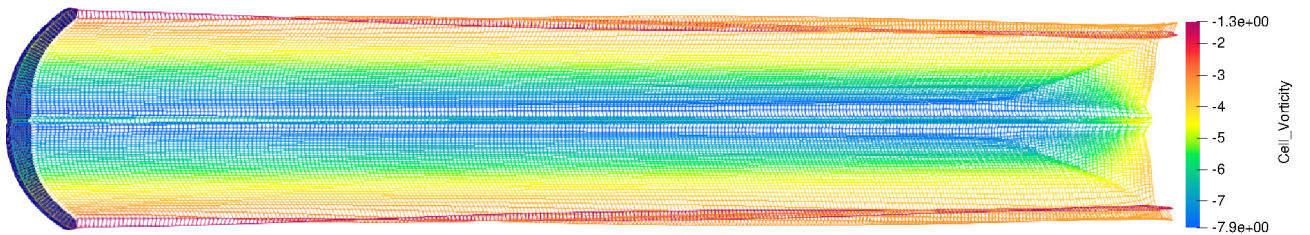


**Figure 7.** MIRAS simulation of the c-shape configuration with the free filament wake model.

#### 145 4.4 LLTunnel

The key elements of the LLTunnel lifting line model are essentially identical to those in MIRAS. However, three main points set LLTunnel and MIARS apart. 1: LLTunnel solves directly for the steady state solution, whereas the MIRAS solution evolves



an unsteady solution. 2: LLTunnel is not a free wake model. The trailed vorticity is assumed to convect downstream directly in the wind/tunnel direction, whereas MIRAS solves for the time true evolution of the force free wake. 3: MIRAS does not have the possibility to enforce walls in the domain in its present version, so the effect of the wall on which the wing is mounted is effectively modeled by modeling also the mirror image of the wing on the other side of the wall. This way there is no flow through the mirror plane, effectively making it a slip wall. This is treated differently in LLTunnel, where any walls in the vicinity of the blade simulated in LLTunnel are simulated using mirror images of the blade and wake vorticity when setting up the influence coefficients of the method (see Katz et al. (2001)). This is also equivalent to enforcing symmetry planes, but it is set up such that more than one wall can be modelled. The added complexity here is that in this case also the mirror images are mirrored. Simulating a wing between two walls therefore result in an infinite row of mirrored blades; the vortex equivalent to the visual impact of standing between two parallel mirrors. In case of two sets of parallel walls, as is the case in the wind tunnel, the result is a full matrix of mirrored vortex elements. Figure 8 show schematically the mirroring method used in LLTunnel.

In the code only the 20 nearest mirror images in each direction was included. The total number of mirrored vortex systems is then  $(20+1+20) \times (20+1+20) - 1 = 1680$ . Using 20 mirror elements to each side was determined as a good number as the difference when resolving in stead the 30 nearest elements had a negligible influence on the results. The blade, and thereby also all mirror elements, is discretized used 80 equidistant elements along the blade span for all LLTunnel calculations shown in this work, as grid studies showed negligible differences in the results for finer resolutions. The effect of point 1 (steady solution) and point 2 (prescribed, non-free wake) is that the method is significantly faster than MIRAS, but that the detailed effects linked to a free wake is not captured. The effect of this will be shown later when comparing the results of MIRAS and LLTunnel. In the context of the present paper, LLTunnel will be used only to assess the difference in modeling a blade on a symmetry wall, which is what is being modelled by all other simulation tools, and modelling a blade in the tunnel, which is what is being measured in the experiments.

#### 4.5 EllipSys3D

Higher fidelity simulations were performed with the three-dimensional computational fluid dynamics code EllipSys3D (Michelsen , 1992, 1994; Sørensen , 1995). EllipSys3D is a finite volume solver for structured grids, and it implements a wide variety of turbulent models. In the present study, the incompressible Reynolds-Averaged Navier-Stokes (RANS) equations were solved, using the  $k-\omega$  SST turbulence model (Menter , 1994). Two distinct sets of simulations were performed. One assumed fully turbulent flow, while the other accounted for a correlation-based transition model (Sørensen , 2009). These two sets of computations are labelled in the present document as `turb` and `trans`, respectively.

A common grid was used for all the EllipSys3D simulations. It was generated in two consecutive steps. First, a structured mesh of the tip surface was generated with the openly available Parametric Geometry Library (PGL) tool (Zahle , 2019). A total of 96 cells were used in the spanwise direction, and the chordwise direction was discretized with 256 cells (with 8 of them lying on the trailing edge). To facilitate the whole grid generation process, the near-root contraction geometry was simplified by assuming a constant chord. Secondly, the surface mesh was radially extruded with the hyperbolic mesh generator Hygrid (Sørensen , 1998) to create a semi-spherical volume grid. A total of 128 cells were used in this process, and the resulting

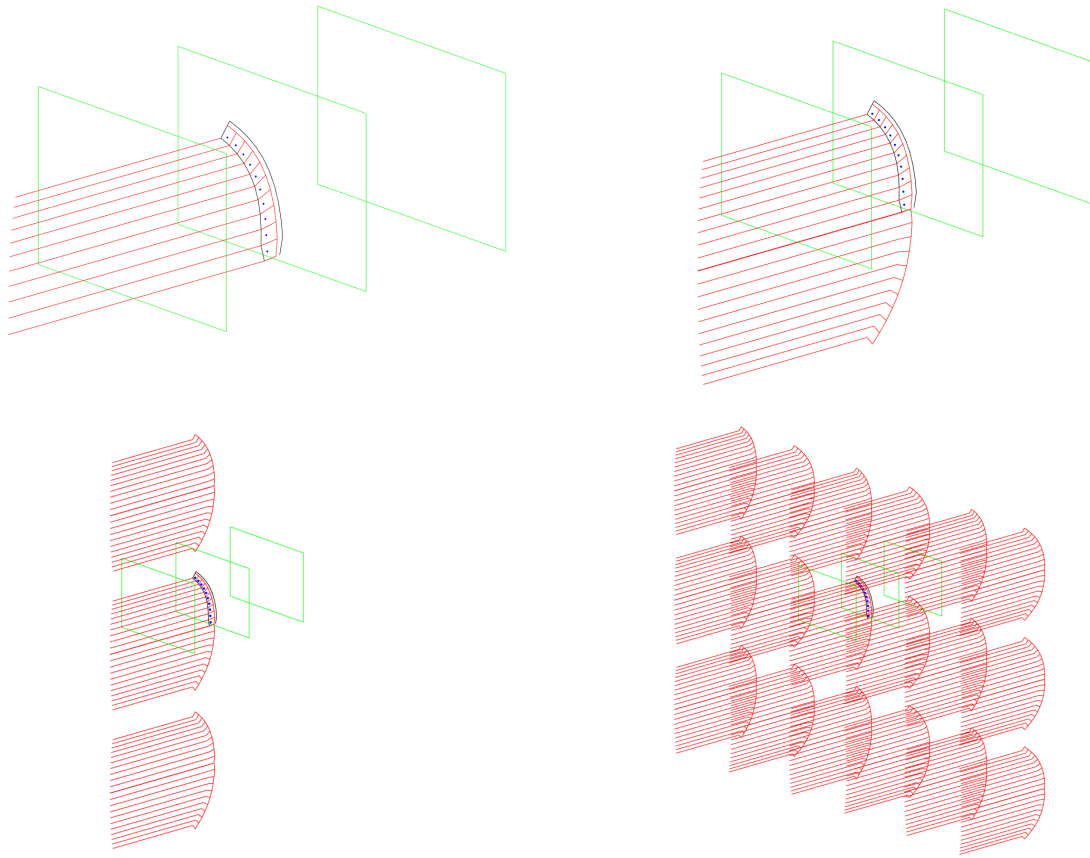


**Figure 8.** Illustration of the use of mirror images model walls. Upper left: Vortex system of physical wing only. The tunnel is outlined in green. Upper right: Vortex system of physical wing and mounting wall vortex systems. This corresponds to what is modelled in all other codes. Lower left: Vortex system of the nearest mirror images from two parallel walls. Lower right: Vortex system from the nearest mirror images due to all four tunnel walls.

outer domain was located approximately 50 m away from the tip. A boundary layer clustering was taken into account, with an imposed first cell height of  $1 \times 10^{-5}$  m, in order to target  $y^+$  values lower than the unity. The resulting volume mesh accounted for a total of 3.7 million cells. An inlet/outlet strategy was followed for the boundary conditions of the outer limit of the domain.

185 The root plane was modeled as a symmetry boundary condition, and the tip itself as a no-slip boundary condition. A sketch of the ensemble of the boundary conditions is depicted in Figure 9, together with a visualization of the mesh. Preliminary studies were performed in order to assess the sensitivity of the grid resolution. It was concluded that the considered discretization is suitable for the type of analysis performed in the framework of the present work.

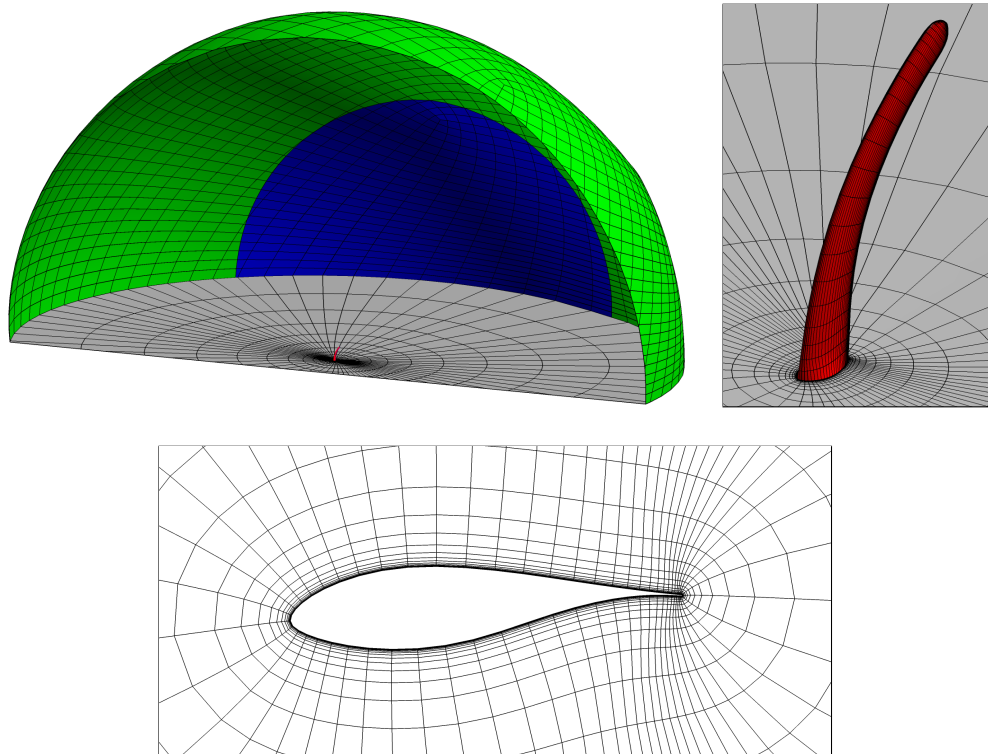


**Figure 9.** Visualization of the EllipSys3D mesh. For clarity, only one out of every four grid lines is shown, and half of the semi-spherical domain is not depicted. Upper row: overview and detail of the boundary conditions distribution (green for inlet, blue for outlet, grey for symmetry and red for wall). Lower row: cross-sectional mesh around the tip shape, taken at one third of its total projected length (starting from the root).

## 5 Comparison of test and simulation results

190 In this section, the main results of the present work are presented. The first subsection lays the foundation for the rest of the investigations by quantifying the difference in aerodynamic forces between the blade mounted on a symmetry wall and a blade mounted between four tunnel walls, like the wind tunnel tests. All following sections contain a comparison of test and simulation results in a progressive manner, going from the most qualitative observations to a quantified comparison. In this way, Section 5.2 discusses first the flow patterns around the tip, comparing the experimental tests with EllipSys3D. These  
 195 observations are complemented by looking at the pressure distributions for both the numerical model and the data acquired during the experiments (Section 5.3). Finally, Section 5.4 shows a comparison of the sectional loads predicted by each of the numerical methods involved in the present study, where the results obtained from the test campaign are also included.

## 5.1 Assessment of tunnel effects

Before the results from the simulation methods can be compared to wind tunnel measurements, we need to quantify the difference in aerodynamic loading between the wing mounted on a wall, like it is modeled in the majority of the computational methods employed in the present study, and the wing mounted in the wind tunnel, which is what is being measured in the experiments. This section uses LLTunnel to assess this difference. Figure 10 shows the clean airfoil data simulation results from the lifting-line codes MIRAS and LLTunnel compared for the four blade sections corresponding to the measurement sections in the experiments.

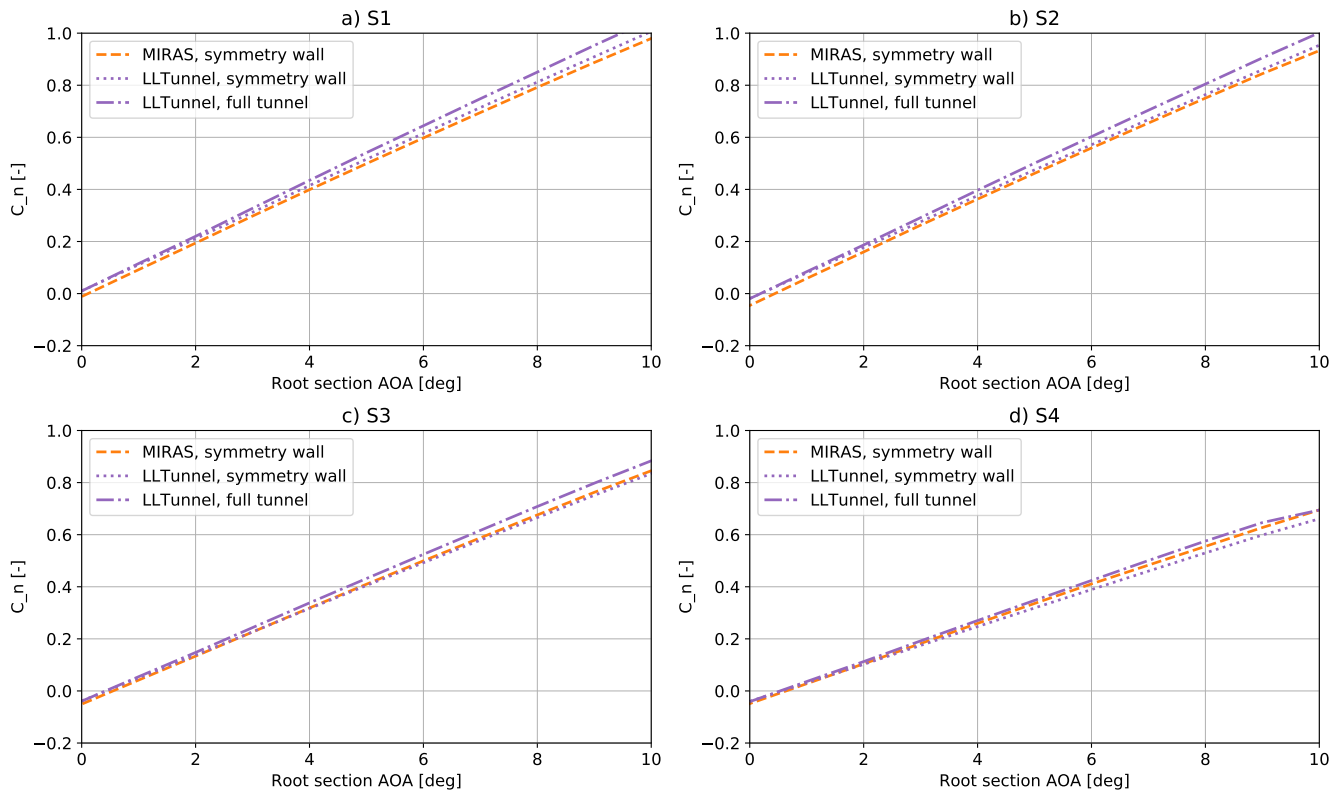


**Figure 10.** The graphs show MIRAS and LLTunnel  $C_n$  values as function of root section AOA for blade sections corresponding to the measurement locations on the wing. Upper left: section 1. Upper right: section 2. Lower left: section 3. Lower right: section 4. MIRAS models the wing on a symmetry wall while LLTunnel models both that configuration and the full tunnel configuration.

The results in the figure show that there is a good agreement between LLTunnel and MIRAS results for the single wall version of the LLTunnel. The relatively small differences between the results can be explained by modeling differences for the two codes. MIRAS includes the free wake effects, which are not included in LLTunnel. On the other hand LLTunnel extends the wake further downstream of the airfoil than MIRAS. The good agreement between the results show that the LLTunnel code is working as intended. The LLTunnel results in the figure also highlights the difference between the wing on a single wall

210 compared to the wing in the full tunnel setup. The results show that the effect of the tunnel is to increase the normal force coefficient slightly for all four sections. This is a result of the upwash caused by the additional mirror images in the tunnel case. The effect of the additional tunnel walls on  $C_n$  at all 4 sections is shown in Figure 11. At a root angle of attack of for instance 6 degrees, the increase in  $C_n$  is of the order of 0.03 from the single wall mounted wing to the full tunnel mounted wing.

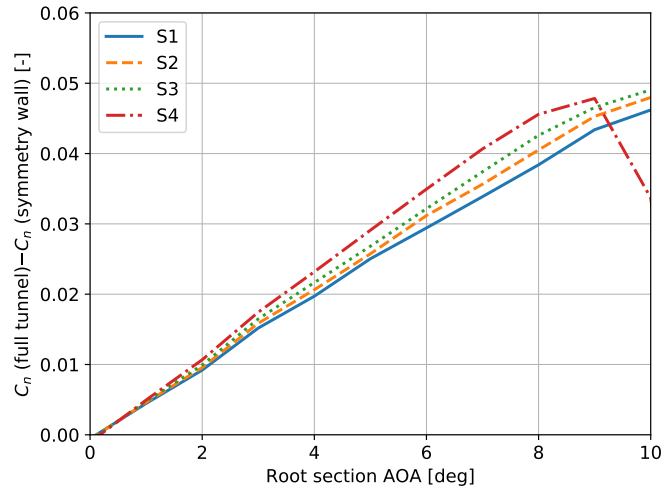


**Figure 11.** The difference in  $C_n$  between the full tunnel configuration and the symmetry wall condition. Computed by the LLTunnel code using clean polars.

The  $C_n$  difference between the full wall effect and the effect of only the mounting wall is small in terms of absolute numbers. Based on this result is assumed that the most of the tunnel effect on the isolated blade is included by simulating the effect of only the mounting wall, as done in all other simulation tools used in this work. This justifies comparing the results from the simulation tools to the experimental data. The difference in  $C_n$  due to the tunnel is assessed as the difference between the 'tunnel' and 'symmetry' results of the LLTunnel results in Figure 10.

## 5.2 Surface flow

220 Figure 12 depicts the visualization of the flow around the suction side  $SS$  of the tip shape, for several angles of attack. Both the snapshot of the experimental campaign which corresponds to the `clean` configuration, and the `trans` results of EllipSys3D are presented. For the latter solver, the flow was visualized via surface-restricted streamlines. For the experiments, the recording relied on chord-wise distributed tufts illuminated by UV light. It should be emphasized that this comparison is merely qualitative, so that the experimental images were not corrected by the camera angle.

225 At an angle of attack of  $0^\circ$ , both the experimental results and the numerical model revealed a horizontal flow pattern. When increasing the AOA to  $10^\circ$ , some of the trailing edge tufts of the outboard part of the experimental test model showed a slight vertical component (from root to tip). This feature could be also observed when comparing the streamlines of EllipSys3D at  $0^\circ$  and  $10^\circ$ . Plausible explanations for this effect could be the pressure difference induced by the swept geometry, or the influ-

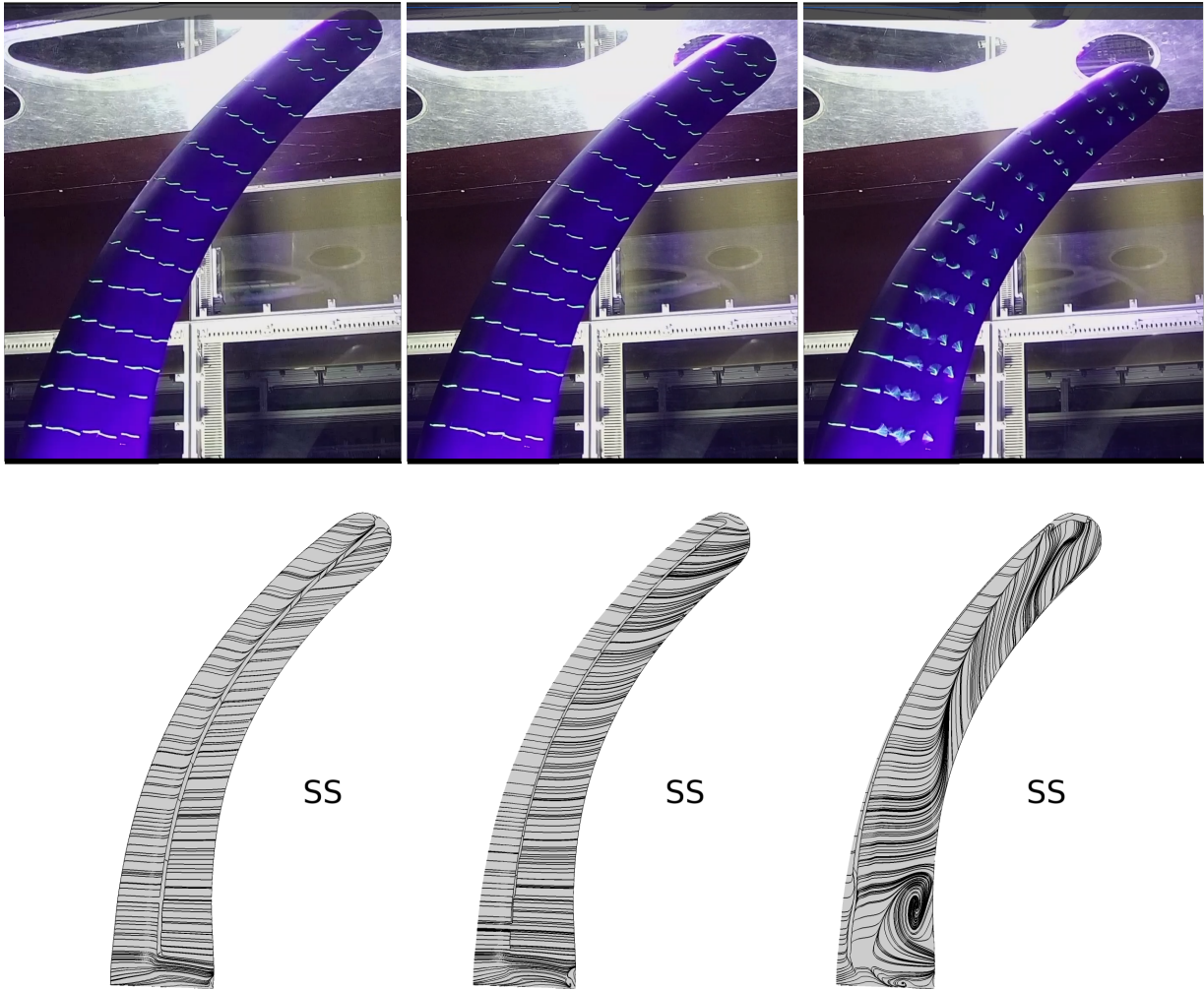


**Figure 12.** Surface flow visualization. Left column:  $0^\circ$  AOA. Middle column:  $10^\circ$  AOA. Right column:  $20^\circ$  AOA. Upper row: experimental results. Lower row: EllipSys3D.

ence of the tip vortex. Finally, both the experiments and the Navier-Stokes solver predicted stall at  $20^\circ$ . While the identification  
 230 of the separation lines for the former case is not straightforward, those seem to be in agreement with the EllipSys3D prediction.  
 It is then concluded that, from a qualitative point of view, the flow around the tip shape predicted by the Navier-Stokes solver  
 is in agreement with the observations of the experimental campaign.

### 5.3 Pressure distribution

Figure 13 depicts the comparison of the pressure coefficient  $C_p$  distributions for the experimental tests and EllipSys3D. The  
 235 obtained pressures have been scaled based on the local freestream velocity. Its value was found by forcing  $C_p$  to be 1.0 for the

lowest pressure of each section. Overall, a good agreement was obtained, especially between the `clean` experiments and the `trans` simulations. For the fully turbulent case, the uncertainties related to the installation of the `zz`-tape on the tip geometry (accurate chord-wise positioning on the 3D geometry) could potentially explain the observed differences. Additionally, it should be reminded that the effects of the `ZZ` tape were included in the CFD simulations through the assumption of a fully turbulent flow. This could omit some three-dimensional effects related to the particular geometry of the employed tape. Regarding the different sections, *S1* is where the discrepancies between the numerical model and the experiments were the highest. That could be explained through the differences in the airfoil geometry at that particular location, since the near-root contraction was replaced by a constant chord evolution in the CFD mesh. While only the  $10^\circ$  angle of attack is included in Figure 13, similar observations could be made for other AOA. It is then concluded that the EllipSys3D predictions are in generally good agreement with the experimental tests. In Section 5.4, a more quantitative comparison is given by showing the numerical integration of the pressure distributions.

#### 5.4 Sectional loads

The measured and simulated normal force coefficients are compared in Figure 14 for the clean configuration and in Figure 15 for the tripped configuration. The numerical results are obtained for the wall mounted configuration, a correction for the effect of the remaining tunnel walls (see Sec. 5.1) is not included. To account for this, all simulated results would have to be moved to slightly higher  $C_n$ , as shown in Fig. 11.

The results from the pure blade element method denoted 'HAWC2' overpredict the normal loading at all sections. As described in Section 4.2 this is due to the missing cross sectional coupling: any change in slope or post stall levels are only due to the projection of the relative velocities into the airfoil cross sections and the following normalization by the wind tunnel speed. All other codes include aerodynamic cross sectional coupling and thus 3D effects, which lead to reduced slopes at all sections in both tripped and clean configurations. The HAWC2 NW and MIRAS computations use the same airfoil data. They produce very similar results at the inboard sections, but differ close to the tip due to the larger sweep angles that are ignored in the trailed vorticity computations in the present HAWC2 NW.

The EllipSys3D results in attached flow are in very close agreement with the MIRAS results except for the most outboard region *S4*, where the slope predicted by EllipSys3D is significantly smaller. This could be explained by the smaller chord lengths and Reynolds numbers outboard, which lead to worse airfoil performance in EllipSys3D but are not taken into account in the airfoil data input to MIRAS.

In almost all cases EllipSys3D and the measurements both qualitatively predict increased maximum normal force coefficients when comparing to the 2D airfoil data read by HAWC2. An exception is section *S2* in the tripped configuration where the maximum measured  $c_n$  is below the 2D value. The stall delay seen in the measurements and EllipSys3D results may be due to the spanwise flow caused by the sweep and proximity to the tip vortex for the outboard sections. Because the EllipSys3D simulations solves the RANS equations, a good representation of the stalled flow region was not expected and thus the behaviour in separated flow will not be discussed further. No 3D correction model for stall delay was used in the codes relying on airfoil data, so also here no accurate prediction of normal force coefficients beyond attached flow is expected.

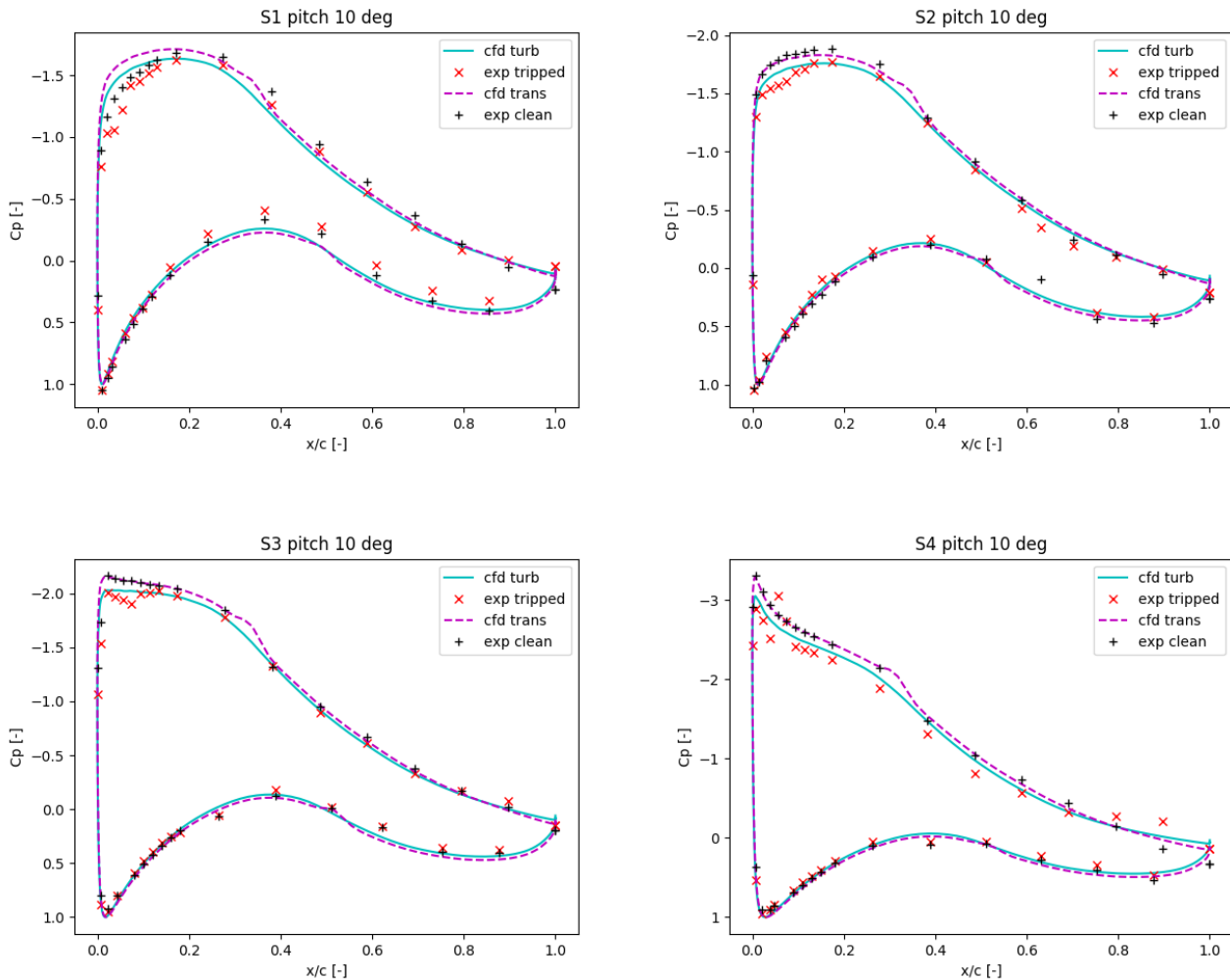


**Figure 13.** Pressure coefficient  $C_p$  distribution, as a function of the normalized chordwise coordinate  $x/c$ . Each graph corresponds to a different section of the tip shape (see Figure 5). EllipSys3D fully turbulent results `cfld turb`, and with transition model `cfld trans`. For the experimental tests, both clean configuration `exp clean` and tripped `exp tripped` are included.

270 For the two inboard sections S1 and S2 all models overpredict  $c_n$  in the attached flow region in the clean and, much more pronounced, in the tripped case. In both cases there is some uncertainty due to the boundary layer at the wind tunnel wall close to the blade root, which was not accounted for in the simulations. This boundary layer may cause the loading to drop towards the root, which could cause additional trailed vorticity and reduced  $c_n$  slopes. This uncertainty can be addressed in future CFD  
 275 be simulated.



As mentioned before, a plausible explanation for the differences between EllipSys3D and the rest of the numerical models was the fact that the latter group used a fixed set of polar data at  $Re=1.78e6$ . Since the wind tunnel operated at Reynolds numbers between 0.6 and 1.5 millions, that could potentially result in significant discrepancies in the loads prediction. To explore this possibility, the authors performed a side study in order to assess the sensitivity of the lift and drag coefficients with regards to a variation of the Reynolds number within the operational range of the wind tunnel. In particular, polar computations were made with the Navier-Stokes code EllipSys2D (a two-dimensional implementation of the solver used for the present project) and the publicly available software Xfoil (Drela , 1989). Two Reynolds number were considered: 0.8e6 and 1.78e6. For both software, the differences in the predicted load coefficients were considerably smaller than the differences between EllipSys3D and the rest of the numerical codes in the present tip study. As an example, at  $AOA=5^\circ$  the Reynolds variation led to relative differences in the order of 2% and -12% for the lift and the drag coefficients respectively. The % differences (especially in  $C_d$ ) could indeed be considered significant, but probably still minor considering the absolute coefficient numbers. It is expected though that the impact of Reynolds number variation is more important in the stall region.

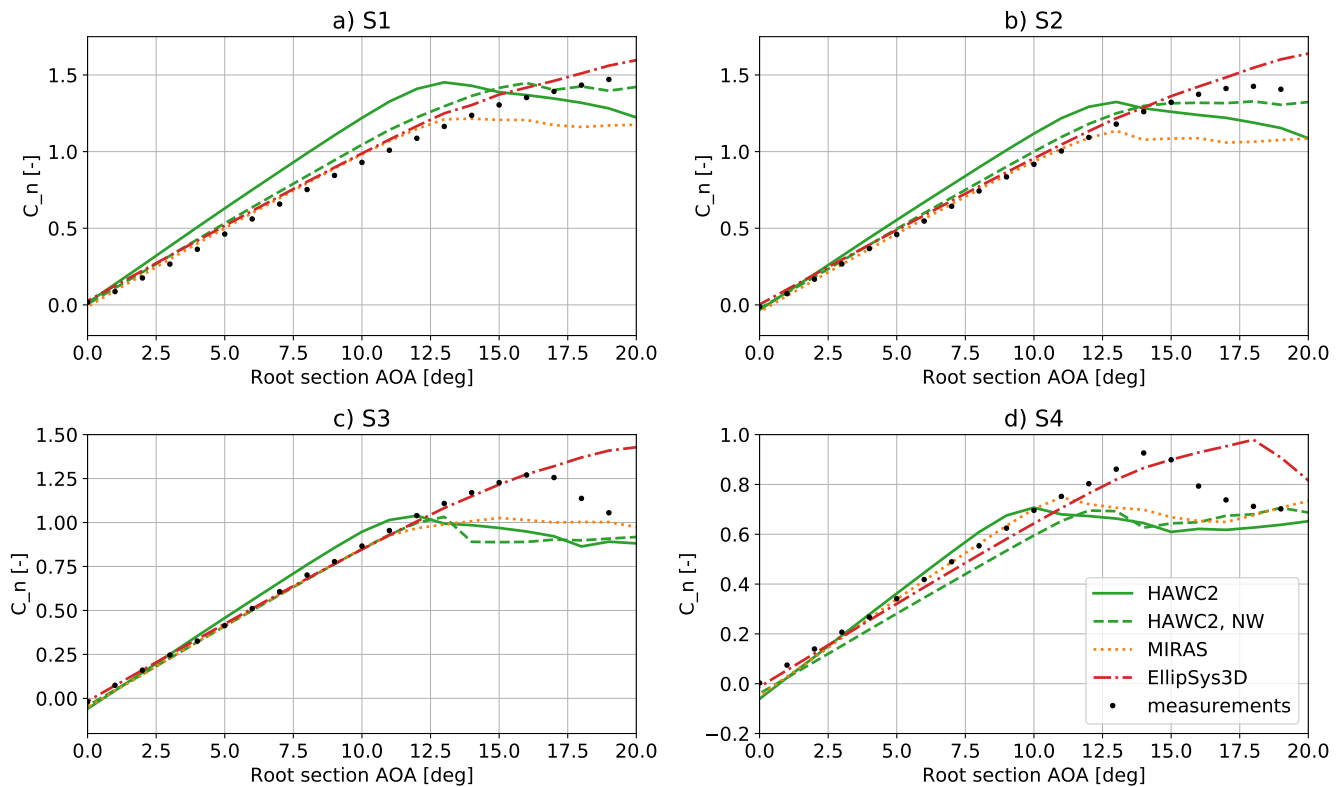


**Figure 14.** Comparison of measured and simulated  $c_n$  at the four instrumented sections, clean airfoils.

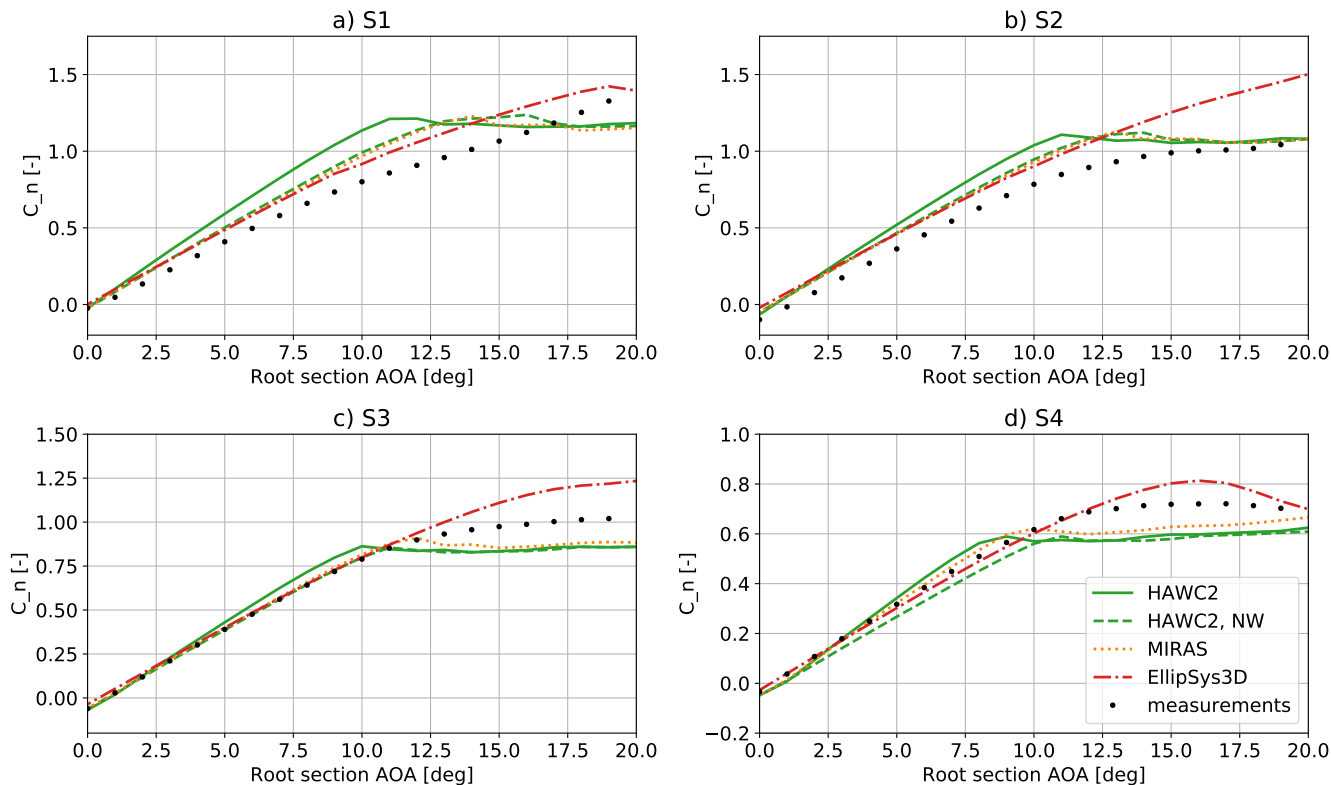


**Figure 15.** Comparison of measured and simulated  $c_n$  at the four instrumented sections, tripped airfoils.

## 6 Conclusions

Wind tunnel tests of an optimized swept tip shape are described. A range of fidelity of aerodynamic models is utilized to simulate the wind tunnel test cases and are compared with the measurement data, namely a blade element model, a near-wake model, a lifting-line free-wake model, and a fully resolved RANS model. In addition to this, the tunnel effects are assessed with a different lifting-line code. Results show qualitative agreement of the surface flow in flow visualization and CFD. Comparing the surface pressure it is seen that there is better agreement for the clean than tripped case at the inboard sections.

When comparing tunnel velocity normalized normal force coefficients as function of geometric root section AOA, important 3D effects cannot be predicted by the blade element model. There is generally good agreement between near wake model, MIRAS, CFD and experiments in attached flow. However the near wake model predicts the outboard section less accurately because the curved geometry is not taken into account, and all codes share an uncertainty close to the root due to the neglected tunnel wall boundary layer. CFD and experiments indicate stall delay, but the quantitative agreement in the post-stall region is only fair. The clean measurements are generally in better agreement with the simulations than the tripped measurements, indicating again a too aggressive tripping. Investigations of the tunnel effect show that the  $C_n$  values in the tunnel are increased

relative to the modelled case of a blade mounted on a symmetry wall. The increase in  $C_n$  at a root AOA of 6 degrees is approx 0.03, justifying the direct comparison of the measured data and the simulation results.

This work has illustrated the challenges associated with testing and modelling a curved tip shape, even at a 2D setup, and quantified the validity of different aerodynamic modeling fidelities. It also serves as a building block for the work on the full  
305 scale rotating field test of the curved tip on the RTR, which will appear soon. Future investigations could focus on clarifying the influence of the wind tunnel wall boundary layer at the root.

*Code and data availability.* Pre/post-processing scripts and data sets available upon request. The codes HAWC2, MIRAS and EllipSys3D are available with a license.

*Author contributions.* Thanasis Barlas performed the tip design optimization, wind tunnel model preparation, instrumentation and testing.  
310 Georg Pirrung contributed to the tip design optimization and performed model simulations. Néstor Ramos García and Sergio González Horcas performed model simulations. Robert Mikkelsen contributed to the preparation of the experiments and their instrumentation. Anders Smærup Olsen contributed to the wind tunnel model testing and data post-processing. Mac Gaunaa performed the study on the wind tunnel corrections. All authors contributed to the writing of this manuscript.

*Competing interests.* No competing interests are present.

315 *Acknowledgements.* This research was supported by the project Smart Tip (Innovation Fund Denmark 7046-00023B), in which DTU Wind Energy and Siemens Gamesa Renewable Energy explore optimized tip designs. The following persons have also contributed to the presented work: Sigurd L. Ildvedsen, Jimmie S. Beckerlee, Helge Aa. Madsen, Flemming Rasmussen, Niels N. Sørensen, Frederik Zahle, Peder B. Enevoldsen and Jesper M. Laursen.

## References

- 320 Hoerner, S.F. and Borst, H.V. (1975). Fluid dynamic lift. Hoerner Fluid Dynamics.
- Katz, J. and Plotkin, A. (2001). Low-Speed Aerodynamics. Cambridge University Press.
- Ai, Q., Weaver, P. M., Barlas, A., Olsen, A. S., Aagaard Madsen , H., and Løgstrup Andersen, T. (2019). Field testing of morphing flaps on  
a wind turbine blade using an outdoor rotating rig. *Renewable Energy*, 133, 53-65.
- Barlas, T., Ramos-García, N., Pirrung, G. R., and González Horcas, S.: Surrogate based aeroelastic design optimization of tip extensions on  
325 a modern 10MW wind turbine, *Wind Energy Science*, 6(2), 491-504. <https://doi.org/10.5194/wes-6-491-2021>.
- Bertagnolio, F. and Sørensen, N. N. and Johansen, J. and Fuglsang, P., Wind turbine airfoil catalogue, 2001, Risoe-R, No. 1280(EN).
- Drela, M. (1989). XFOIL: An Analysis and Design System for Low Reynolds Number Airfoils. In *Low Reynolds aerodynamics*, p 1-12.  
Doi: 10.1007/978-3-642-84010-4\_1
- Gaunaa, M. and Johansen, J., 2007, Determination of the maximum aerodynamic efficiency of wind turbine rotors with winglets, *Journal of*  
330 *Physics: Conference Series* (online), 75(1):012006.
- Gertz, D. and Johnson, D. and Swytink-Binnema, N., 2012, An evaluation testbed for wind turbine blade tip designs - Winglet results, *Wind*  
*Engineering*, 136(4):389-410.
- Hansen, T. H. and Mühle, F., 2018, Winglet optimization for a model-scale wind turbine, *Wind Energy*, 21(8):634-649.
- Horcas, S.G. and Barlas, T. and Zahle, F. and Sørensen, N.N., 2020, Vortex induced vibrations of wind turbine blades: Influence of the tip  
335 geometry, *Physics of Fluids*, 32(6):065104.
- Johansen, J. and Sørensen, N. N., 2006, Aerodynamic investigation of winglets on wind turbine blades using CFD, Technical report, Risoe-R  
1543(EN).
- Jones, B. M. (1936). The measurement of profile drag by the pitot traverse method. ARC RM 1688.
- Larsen, T. J. and Hansen, A. M., 2007, How2HAWC2, Technical report, DTU R-1597(EN).
- 340 Li, A. and Pirrung, G. R. and Madsen, H. Aa. and Gaunaa, M. and Zahle, F., 2018, Fast trailed and bound vorticity modeling of swept wind  
turbine blades, *Journal of Physics: Conference Series*, 1037(6):062012.
- Li, A. and Gaunaa, M. and Pirrung, G. R. and Ramos-García, N. and González Horcas, S. (2020). The influence of the bound vortex on  
the aerodynamics of curved wind turbine blades. *Journal of Physics: Conference Series*. <https://iopscience.iop.org/article/10.1088/1742-6596/1618/5/052038>
- 345 Aagaard Madsen , H., Barlas, A., and Løgstrup Andersen, T. (2015). Testing of a new morphing trailing edge flap system on a novel  
outdoor rotating test rig. In *Scientific Proceedings. EWEA Annual Conference and Exhibition 2015* (pp. 26-30). European Wind Energy  
Association (EWEA).
- Menter, F. R. (1994). Two-equation eddy-viscosity turbulence models for engineering applications. *AIAA Journal*, 32(8), 1598–1605. Doi:  
10.2514/3.12149
- 350 Michelsen, J. A. (1994). Block structured multigrid solution of 2D and 3D elliptic PDEs. Report AFM 94-06. Risø National Laboratory,  
Roskilde.
- Michelsen, J. A. (1992). Basis3D—a platform for development of multiblock PDE solvers. Report AFM 92-05. Risø National Laboratory,  
Roskilde.
- Pirrung, G. R., Aagaard Madsen , H., Kim, T., and Heinz, J. C. (2016). A coupled near and far wake model for wind turbine aerodynamics.  
355 *Wind Energy*, 19(11), 2053–2069.

- Pirrung, G. R., Riziotis, V., Madsen, H. Aa., Hansen, M., and Kim, T. (2017). Comparison of a Coupled Near and Far Wake Model With a Free Wake Vortex Code. *Wind Energy Science*, 2, 15-33.
- Pirrung, G. R., Madsen, H. Aa., Schreck, S. (2017b). Trailing vorticity modeling for aeroelastic wind turbine simulations in stand still. *Wind Energy Science* 2 (2), 521-532
- 360 Ramos-García, N. and Sørensen, J. N. and Shen, W. Z. (2016), Three-dimensional viscous-inviscid coupling method for wind turbine computations, *Wind Energy*, 19(1):67-93.
- Ramos-García N. , Hejlesen M. M., H. J. and Sørensen, J. N. and Walther, J. H. 2017. Hybrid vortex simulations of wind turbines using a three-dimensional viscous-inviscid panel method, *Wind Energy*, 20(11):1871-1889.
- Ramos-García , N. and Spietz, H. J. and Sørensen, J. N. and Walther, J. H., 2019 Vortex simulations of wind turbines operating in atmospheric conditions using a prescribed velocity-vorticity boundary layer model, *Wind Energy*, 21(11):1216-1231.
- 365 Ramos-García , N. and Sessarego, M. and González Horcas, S., 2020, Aero-hydro-servo-elastic coupling of a multi-body finite-element solver and a multi-fidelity vortex method. *Wind Energy*. <http://dx.doi.org/10.1002/we.2584>
- Sørensen, N. N. (1995). General purpose flow solver applied to flow over hills. PhD thesis. Risø National Laboratory, Roskilde.
- Sørensen, N. N. (1998). HypGrid2D—a 2-D mesh generator. Technical report R-1035, Risø National Laboratory, Roskilde.
- 370 Sørensen, N. N. (2009). 3D CFD computations of transitional flows using DES and a correlation based transition model. Technical report, Risø National Laboratory, Roskilde.
- Veers, P. et al, 2019, Grand challenges in the science of wind energy, *Science*, 366(6464):443-+.
- M. P. Scully and J. P. Sullivan. Technical Report 183, MIT DSR No. 73032, Massachusetts Institute of Technology Aerophysics Laboratory. Helicopter Rotor Wake Geometry and Airloads and Development of Laser Doppler Velocimeter for Use in Helicopter Rotor Wakes
- 375 Zahle, F. (2019). Parametric Geometric Library (PGL). <https://gitlab.windenergy.dtu.dk/frza/PGL>